Electronic Supplementary Information

A strategy to control grain boundary density and Cu^+/Cu^0 ratio of Cu-based catalysts for efficient electroreduction of CO_2 to C2 products

Chunjun Chen,[a,b] Xiaofu Sun,[a,b*] Xupeng Yan,[a,b] Yahui Wu,[a,b] Mingyang Liu,[a,b] Shuaishuai Liu,[a,b] Zhijuan Zhao,[a] Buxing Han[a,b,c,d*]

[a]Beijing National Laboratory for Molecular Sciences, Key Laboratory of Colloid and Interface and Thermodynamics, Institute of Chemistry, Chinese Academy of Sciences, Beijing 100190, China

[b]School of Chemistry and Chemical Engineering, University of Chinese Academy of Sciences, Beijing 100049, China

[c]Physical Science Laboratory, Huairou National Comprehensive Science Center, No. 5 Yanqi East Second Street, Beijing 101400, China

[d]Shanghai Key Laboratory of Green Chemistry and Chemical Processes, School of Chemistry and Molecular Engineering, East China Normal University, Shanghai 200062, China

Experimental Section

Materials: Ethanol, orthophosphoric acid (85%), sodium hydroxide (NaOH), potassium persulfate ($K_2S_2O_8$) and acetone were obtained from Sinopharm Chem. Reagent Co. Ltd. Cu film, $H_2{}^{18}O$, Potassium bicarbonate ($KHCO_3$) and Nafion N-117 membrane (0.180 mm thick, ≥0.90 meg/g exchange capacity) were purchased from Alfa Aesar China Co., Ltd. N_2 and CO_2 (99.999%) were provided by Beijing Analytical Instrument Company.

Synthetic procedures for $Cu(OH)_2$: $Cu(OH)_2$ were prepared through modified chemical immersion method.[S1] In a typical procedure, a Cu foil (10 mm×10 mm) was mechanically polished, then electropolished in 85 wt% phosphoric acid at 2.0 V vs. Ag/AgCl for 500 s. Polished Cu foils were washed with deionized water, and immersed into a chemical bath immediately. The bath was filled with sodium hydroxide (4.0 g), potassium persulfate (1.62 g) and deionized water (40 mL). After 10 h, $Cu(OH)_2$ film was obtained, and then it was washed with deionized water.

Synthetic procedures for R-Cu-x: Firstly, the muffle furnace was preheated to 500 °C with a heating rate of 10 °C min^{-1} and maintained at 500 °C. Then the obtained $Cu(OH)_2$ was quickly put in the muffle furnace with 500 °C by crucible tongs, and taken out quickly after calcining for several minutes. The $Cu(OH)_2$/CuO composites were prepared. For clarity, Composites-x refers to $Cu(OH)_2$/CuO film, and x represents the the minutes of calcination. Finally, Composites-x were electrochemically reduced at -2.0 V vs. RHE for 500 s, leading to the formation of R-Cu-x.

Materials characterizations: The microstructures of the catalysts were characterized by scanning electron microscope (SEM, HITACHI S-4800) and transmission electron microscopy (TEM, JEOL JEM-2100F) equipped with EDS. X-ray photoelectron spectroscopy (XPS) study was carried out on the Thermo Scientific ESCALab 250Xi using a 200W Al-Kα radiation. In the analysis chamber, the base pressure was about 3×10^{-10} mbar. Typically, the hydrocarbon C1s line at 284.8 eV from adventitious carbon was used for energy referencing. X-Ray diffraction (XRD) analysis of the samples were performed on a Rigaku D/max-2500 X-ray diffractometer with Cu-Kα radiation (y = 0.15406 nm) and the scan speed was 5°/min. The Raman spectra of the samples were obtained at room temperature in flamesealed capillary on a FT Bruker RFS 106/S spectrometer, equipped with a 514 nm laser, in the region from 1000 to 100 cm^{-1} with a resolution of 2 cm^{-1}.

Semi-in-situ X-ray photoelectron spectroscopy. In order to detect accurately the valence state of Cu, the XPS samples were processed in a glove box. After electrolysis, the electrode plate was soaked in acetone solution, and put into the glove box immediately. The obtained electrode plate was cut into 3 × 3 mm and glued on a support. The support could be evacuated into vacuum to prevent the samples to be oxidized by the air. The subsequent testing

processes were the same as the common XPS.

Electrochemical study: All the experiments of CO_2 reduction were carried out on the electrochemical workstation (CHI 660E, Shanghai CH Instruments Co., China). Linear sweep voltammetry (LSV) scans were conducted in a single compartment cell with a three electrodes configuration, which consisted of working electrode, a platinum gauze as counter electrode, and Ag/AgCl (saturated KCl solution) as reference electrode. Prior to experiment, the electrolyte was bubbled with N_2 or CO_2 at least 30 min to form N_2 or CO_2 saturated solution. LSV measurement in gas-saturated electrolytes was conducted in the potential range of 0 V to -1.2 V versus RHE at a desired 20 mV s^{-1} sweep rate. All potentials cited in this work were referenced to the RHE. The potentials were converted to RHE using the formulas E (vs RHE) = E (vs Ag/AgCl) + 0.197 V + 0.0591 × pH.

The electrolysis experiments were conducted at 25 °C in a H-type cell[S2] with a working cathode, a counter anode (platinum gauze), and a reference electrode (Ag/AgCl with saturated KCl). In the experiment, Nafion-117 membrane was used as proton exchange membrane to separate the cathode and anode compartments. $KHCO_3$ aqueous solution (0.1 M) were used as electrolyte. In each experiment, the amount of electrolyte was 30 mL. Before the electrolysis experiment, the catholyte was bubbled with CO_2 for 30 min under stirring and the electrolysis was carried out under a steady stream of CO_2 (20 sccm).

Product analysis. The gaseous product of electrochemical experiments was collected using a gas bag and analyzed by gas chromatography (GC, HP 4890D), which was equipped with TCD detectors using argon as the carrier gas. The liquid product was analyzed by ^{1}H NMR (Bruker Avance III 400 HD spectrometer) in deuteroxide with phenol as an internal standard.

Calculations of Faradaic efficiencies of gasous and liquid products.

liquid products:

After electrolysis, a certain amount of phenol solution was added to the electrolyte as the internal standard. Because the concentration of phenol was known, the moles of liquids products can be calculated from integral areas and calibration curves.

The Faradaic efficiency of liquid product is:

$$FE = \frac{moles\ of\ product}{Q\ /\ nF} \times 100\%$$

(Q: electric quantity; F: Avogadro constant; n: transfer electron number)

Gasous products:

From the GC peak areas and calibration curves for the TCD detector, we can obtain the V % of gasous products .

Since the flow rate of the CO_2 was constent, the moles of gasous products can be calculated. The Faradaic efficiency of gasous product is:

$$FE = \frac{moles\ of\ product}{Q\ /\ nF} \times 100\%$$

(Q: electric quantity; F: Avogadro constant; n: transfer electron number)

Electrochemical impedance spectroscopy (EIS) study: The EIS measurement was carried out in $KHCO_3$ aqueous solution (0.1 M) at an open circuit potential (OCP) with an amplitude of 5 mV of 10^{-2} to 10^5 Hz.

Double-layer capacitance (C_{dl}) measurements: The electrochemical active surface area is proportional to C_{dl} value. C_{dl} was determined by measuring the capacitive current associated with double-layer charging from the scan-rate dependence of cyclic voltammogram (CV). The CV ranged from -0.6 V to -0.7 V vs. Ag/AgCl. The C_{dl} was estimated by plotting Δj (j_a-j_c) at -0.65 V vs Ag/AgCl against the scan rates, in which j_a and j_c were the anodic and cathodic current density, respectively. The scan rates were 20, 30, 40, 50 and 60 mV s^{-1}.

The ECSA of the working electrodes could be calculated according to the following equation: ECSA = R_fS, where S was the real surface area of the working electrode and R_f was the roughness factor of the working electrode. Notably, S was generally equal to the geometric area of working electrode (in this work, S = 1 cm^2). The roughness factor (R_f) can be calculated by the relation $R_f = C_{dl}/a$. The roughness factor of R-$Cu(OH)_2$ was defined to be 1, then the normalized current density can be calculated according to roughness factor of different catalysts.

Measurement of grain boundary (GB) surface densities[S3]:

The method described below was chosen to provide an accurate measurement of the relative GB surface density. We chose ~30 nanoparticles from high resolution TEM images for each of R-Cu-x sample (as-deposited R-$Cu(OH)_2$, R-Cu-2, R-Cu-5, R-Cu-10 and R-Cu-20). For each of these NP images, the length of the GBs (if present) and the particle area were measured.

L_i = GB length in TEM image for particle $_i$

A_i = particle area in TEM image for particle i

L_i was determined by measuring the length of a line traced over the GB image. Most particles had GBs, so the GBs were readily identified. To measure A_i, each particle image was approximated either as a circle, a rod with semi-circular caps, or a combination of these shapes (see below). The image was fit to two shapes, one slightly smaller than the image and one slightly larger. A_i was taken to be the average of the areas of these two fits. This method of measuring the particle area in the TEM image was chosen because the values could readily be converted into 3D particle surface areas. The measured values L_i and A_i were converted to the 3D GB surface lengths and the 3D

particle surface areas using conversion factors derived from the assumption that the particles have round morphologies:

C_L = conversion factor from measured GB length L_i to 3D GB surface length;

C_A = conversion factor from measured particle area A_i to 3D particle surface area.

The 3D GB surface length was approximated as the circumference of a circle with diameter L_i:

3D GB surface length =πLi, so conversion factor $C_L = \pi$

The value for C_A depends on the particle shape as illustrated in the following examples:

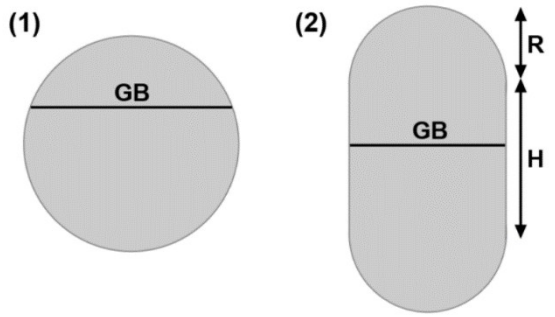

(1) Spherical shape, with radius R and measured GB length L

3D GB surface length = πL

3D particle surface area = $4\pi R^2$, so conversion factor $C_A = 4$ for this model.

(2) Cylindrical shape with length H, hemispherical ends of radius R, and GB length L

3D GB surface length =πL

3D particle surface area = $4\pi R^2 + 2\pi RH$, so CA = $\frac{4\pi R^2 + 2\pi RH}{\pi R^2 + 2RH} = 4 - \frac{4-\pi}{1+\frac{\pi R}{2H}}$ for this model.

(3) Other complicated geometries (a small fraction) could be divided into parts that fit simple models such as sphere, hemisphere, and cylinder.

Using all of the measured values for L_i and A_i for all of the NPs imaged, and the appropriate conversion factors, the 3D GB surface densities were calculated as follows:

$$\text{3D GB surface density} = \frac{\sum_{All\ particles} GB\ Surface\ Length}{\sum_{All\ particles} Surface\ Area} = \frac{\sum_i \pi L_i}{\sum_i C_A A_i}$$

Supplementary Figures

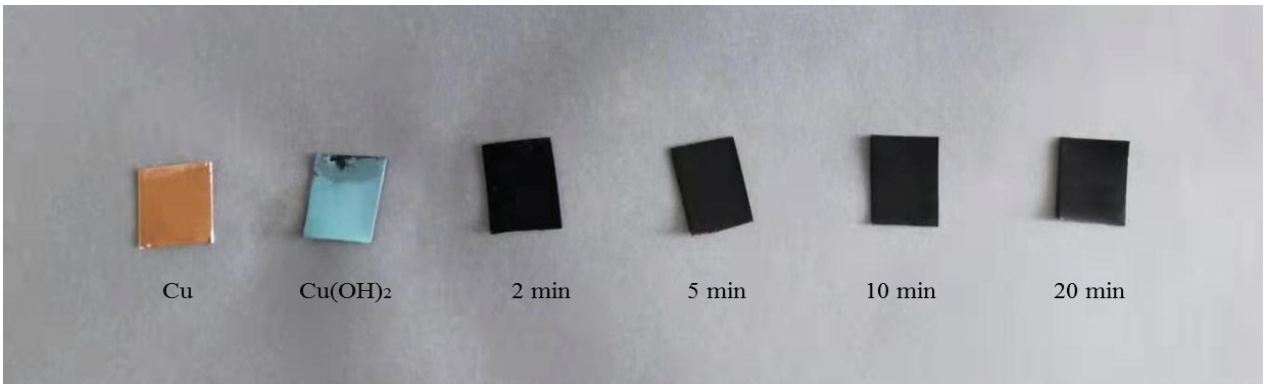

Figure S1. The optical pictures of the samples.

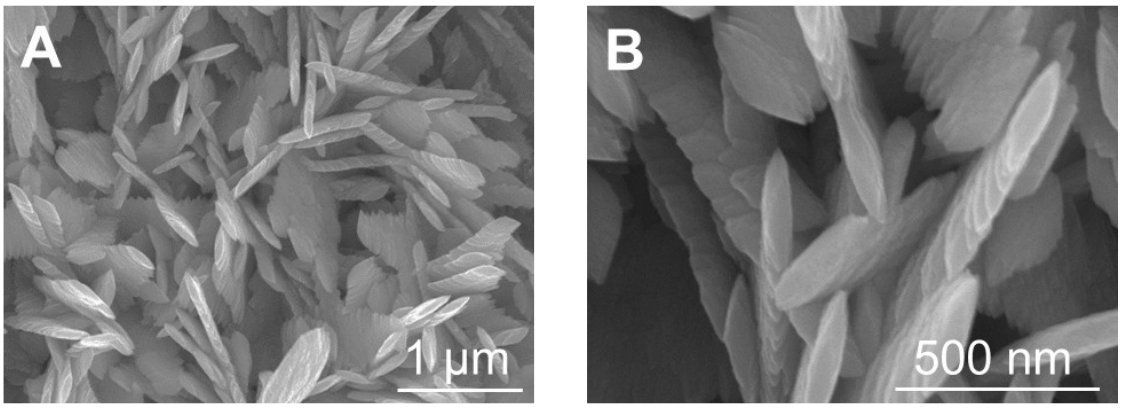

Figure S2. SEM images of $Cu(OH)_2$.

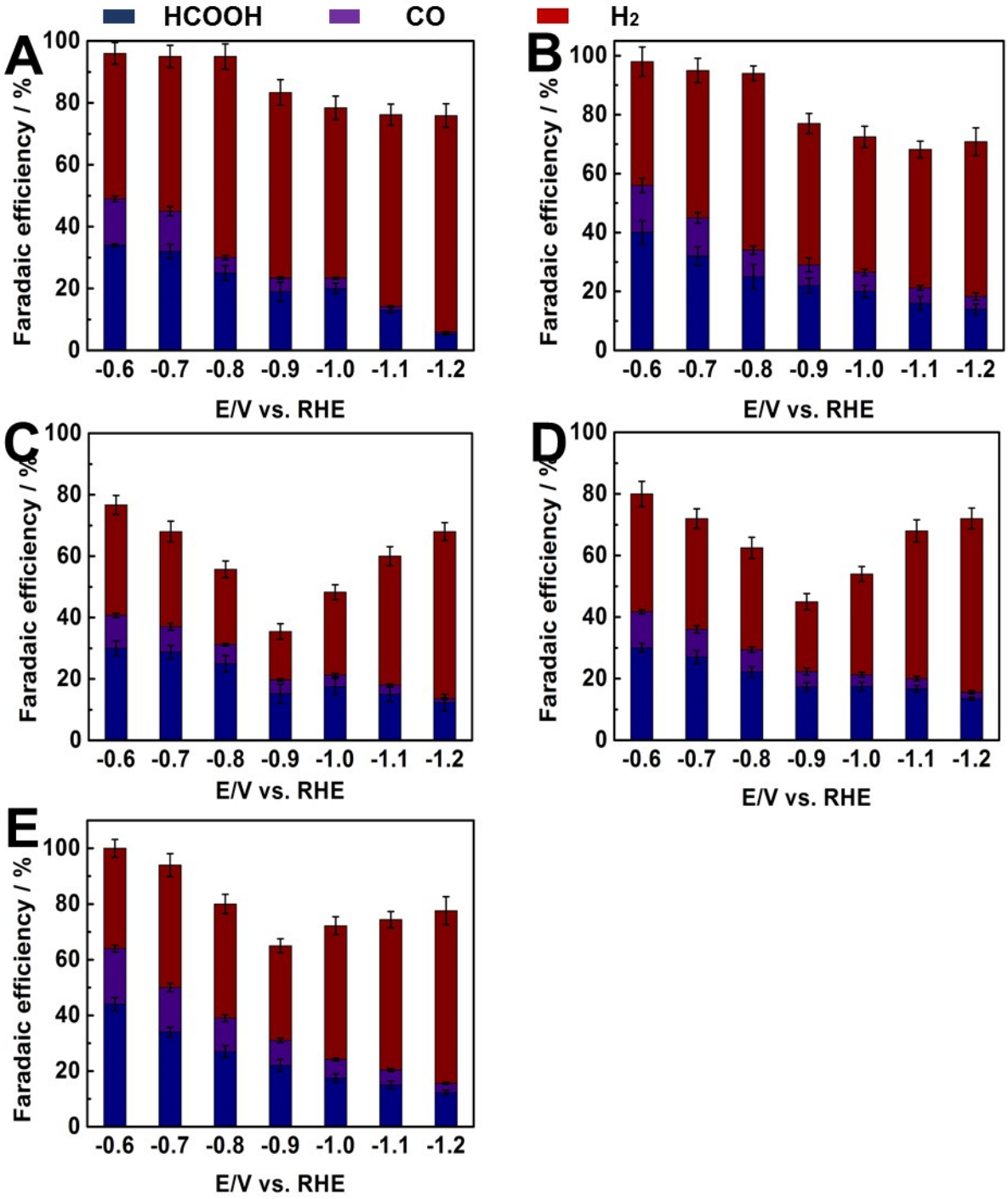

Figure S3. The distribution of H_2 and C1 products for R-Cu-x: R-$Cu(OH)_2$ (A), R-Cu-2 (B), R-Cu-5 (C), R-Cu-10 (D) and R-Cu-20 (E).

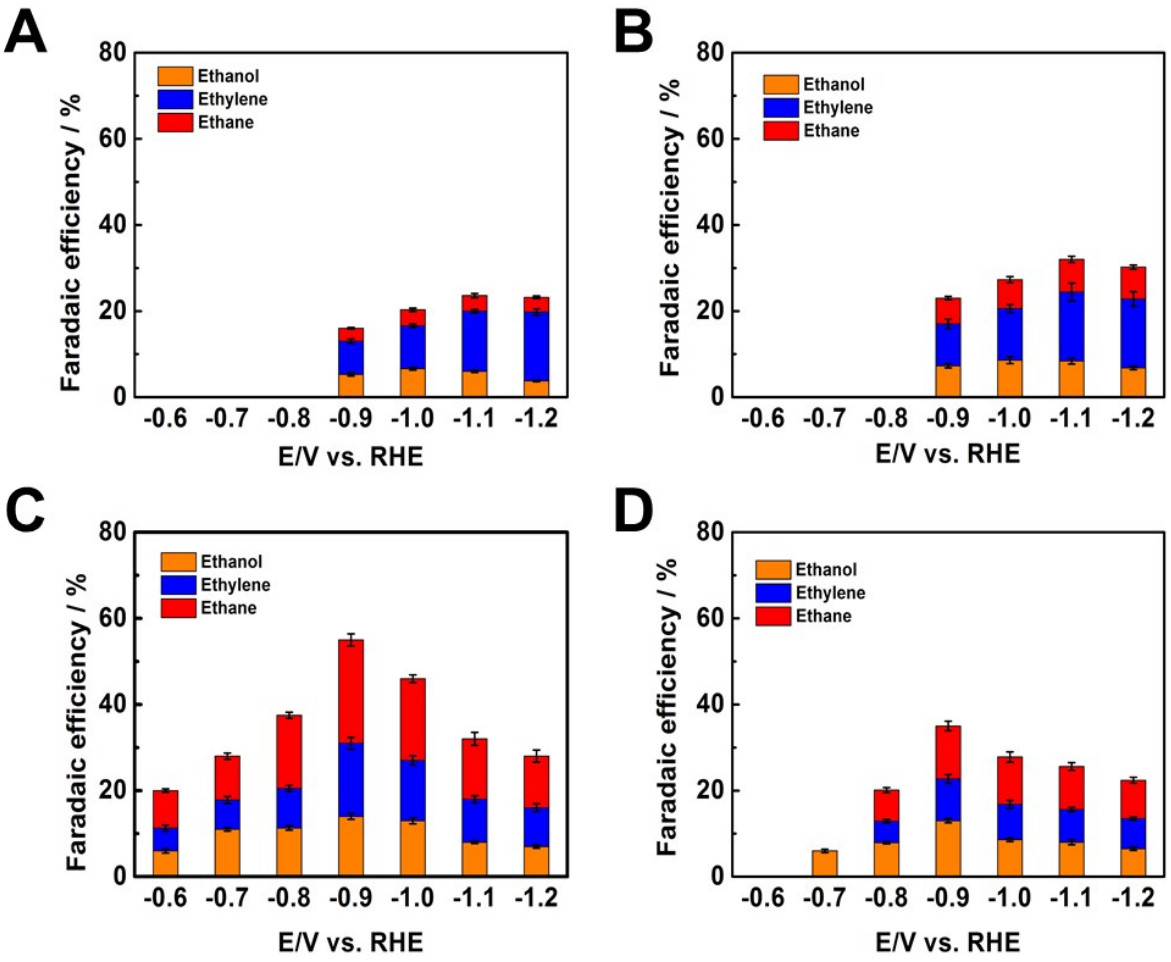

Figure S4. The distribution of C2 products for R-Cu-x: R-Cu$(OH)_2$ (A), R-Cu-2 (B), R-Cu-10 (C) and R-Cu-20 (D).

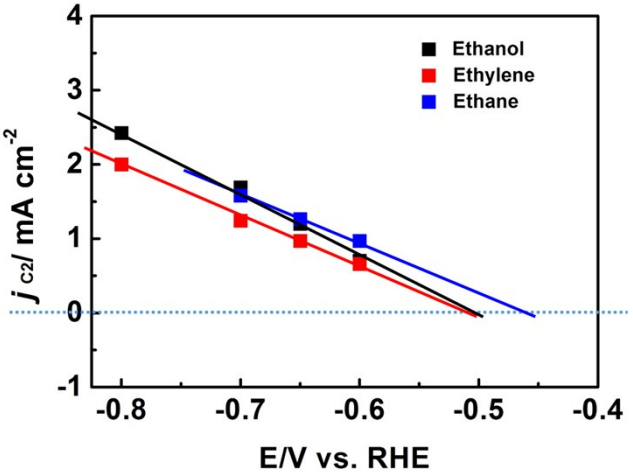

Figure S5. The onset potentials of C2 products for R-Cu-5, obtained from the tangent line method.

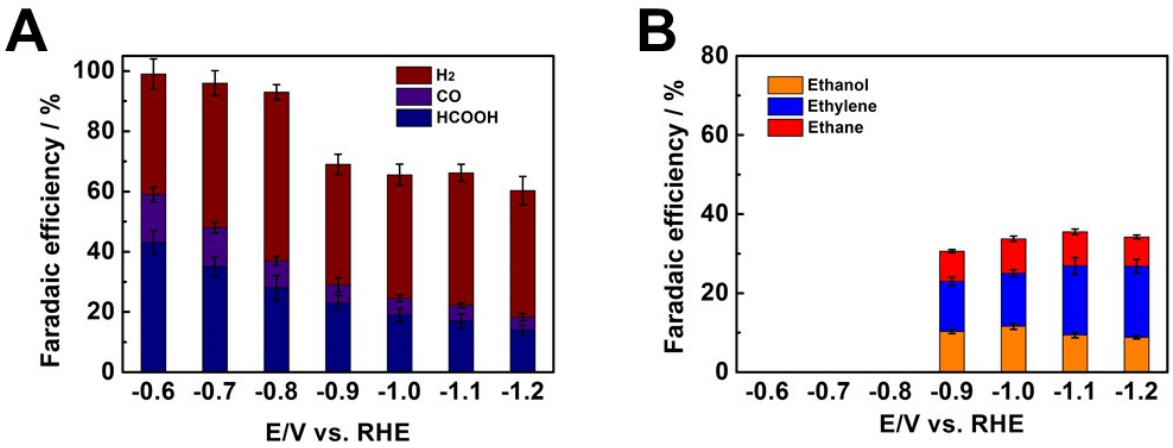

Figure S6. (A) The distribution of H_2 and C1 products for R-Cu-5 (400); (B) The distribution of C2 products for R-Cu-5 (400). R-Cu-5 (400) represents the material calcined at 400 °C for 5 min.

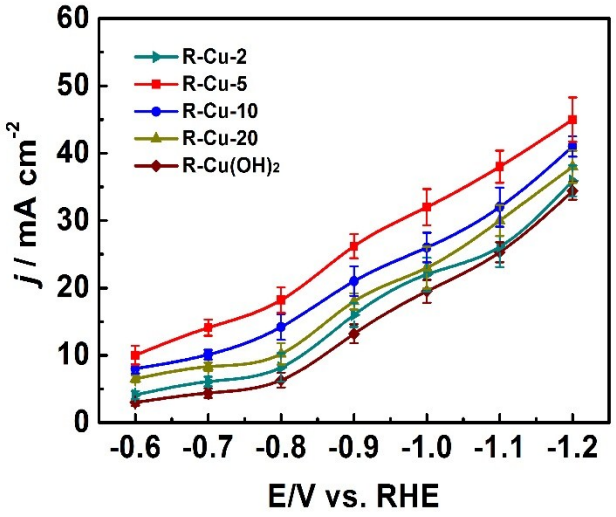

Figure S7. The total current density over different R-Cu-x.

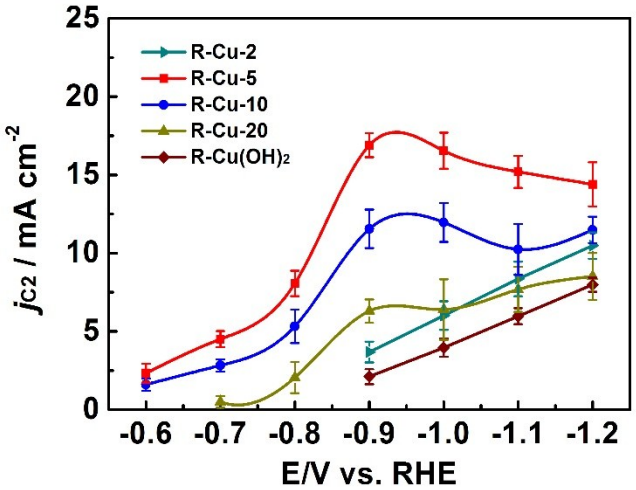

Figure S8. The current density for C2 products over different R-Cu-x.

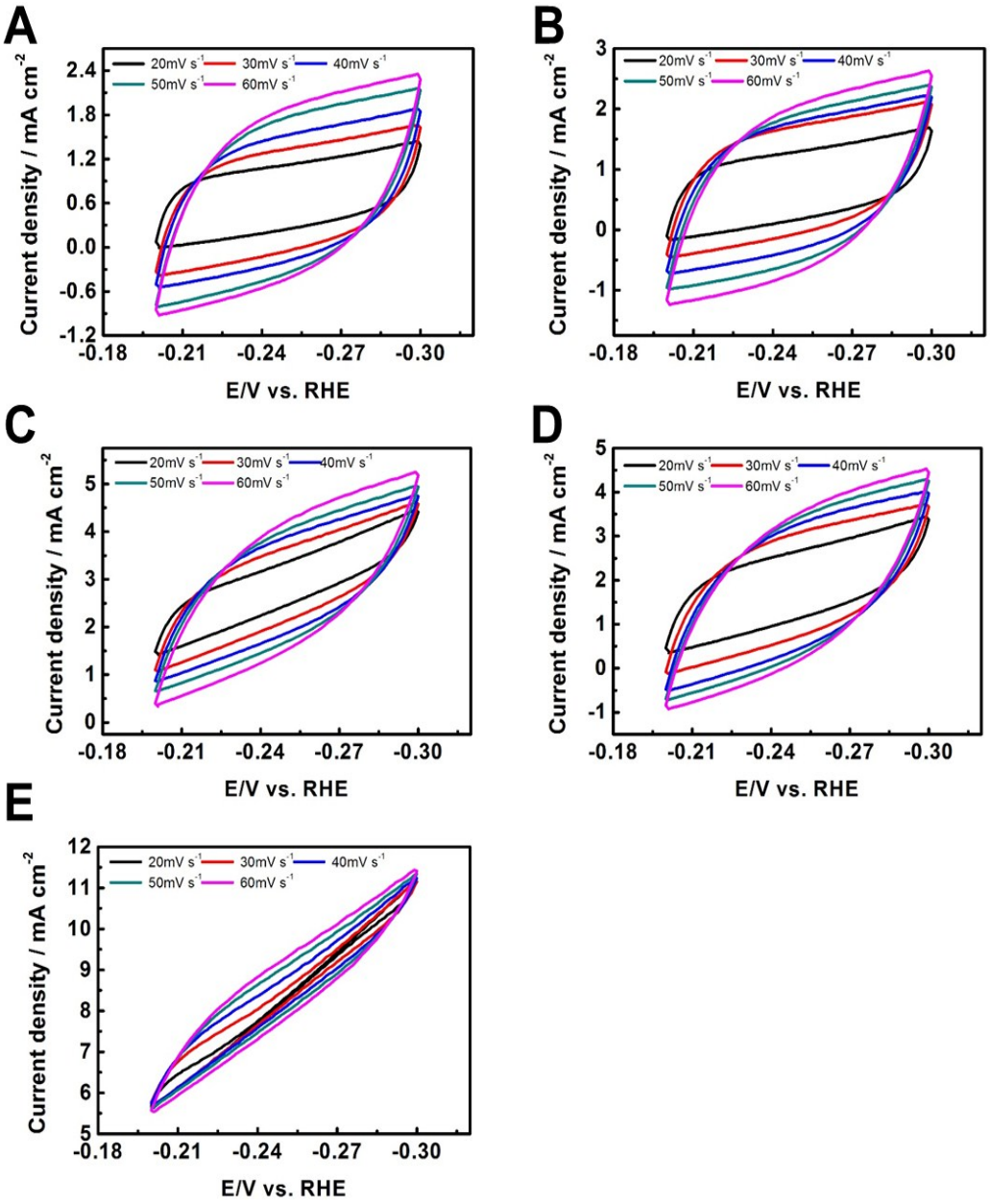

Figure S9. The cyclic voltammetry results on R-Cu-x at different scan rates: R-Cu$(OH)_2$ (A), R-Cu-2 (B), R-Cu-5 (C), R-Cu-10 (D) and R-Cu-20 (E).

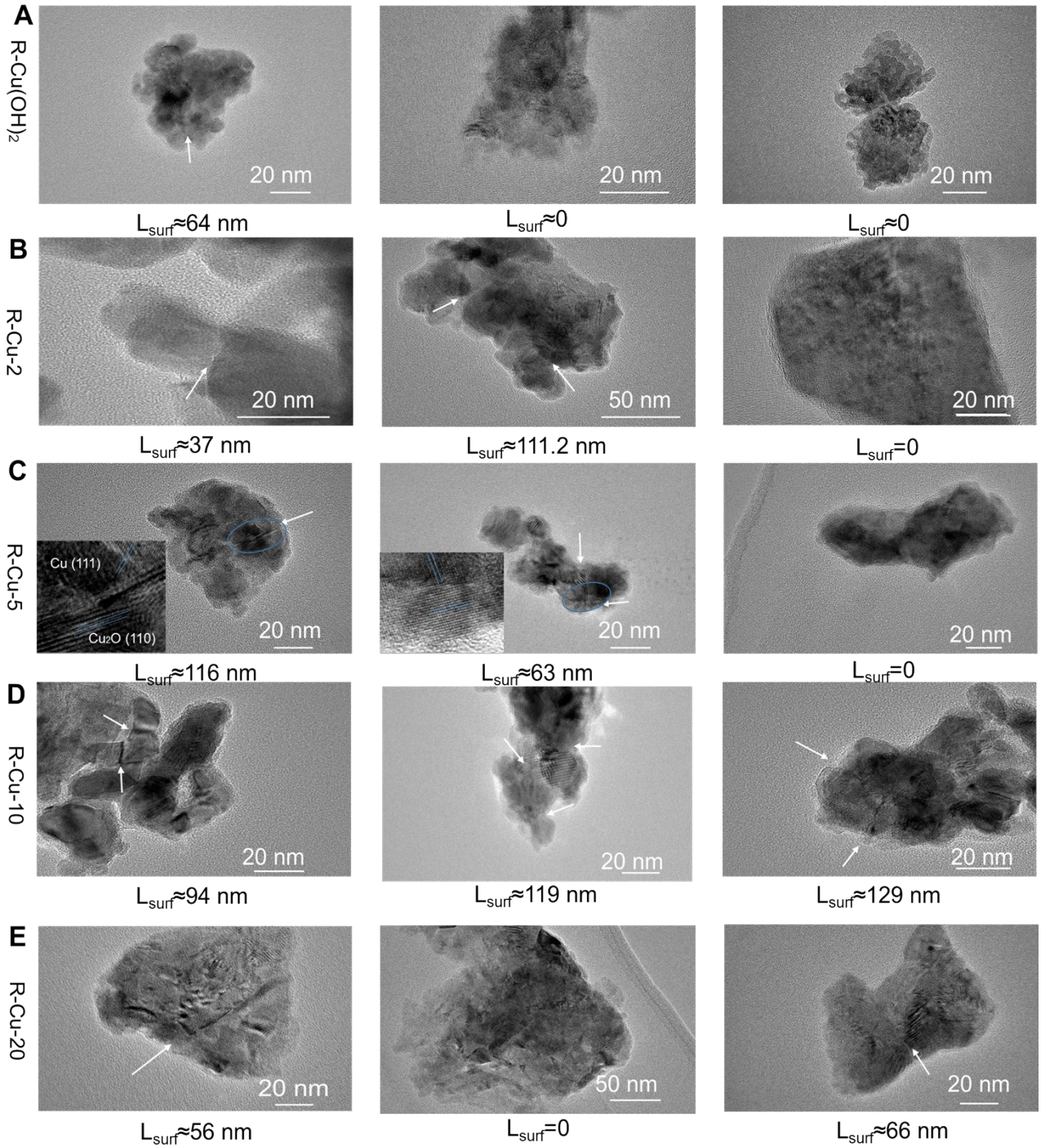

Figure S10. HR-TEM images of different R-Cu-x.

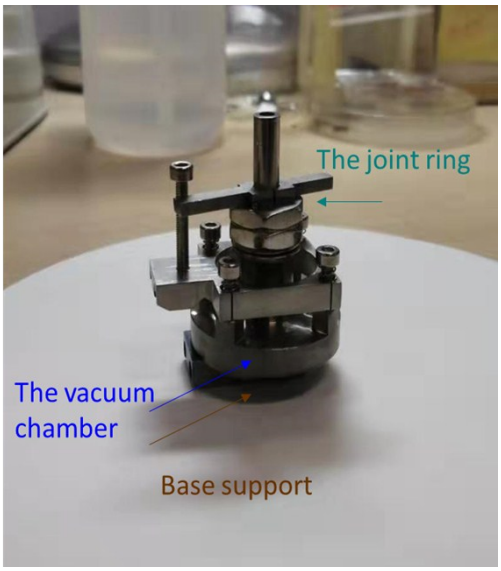

Figure S11. The optical pictures of the semi-in-situ XPS cell. The obtained electrode plate was cut into 3 × 3 mm and glued on the support. The vacuum chamber could be evacuated into vacuum to prevent the samples to be oxidized by the air.

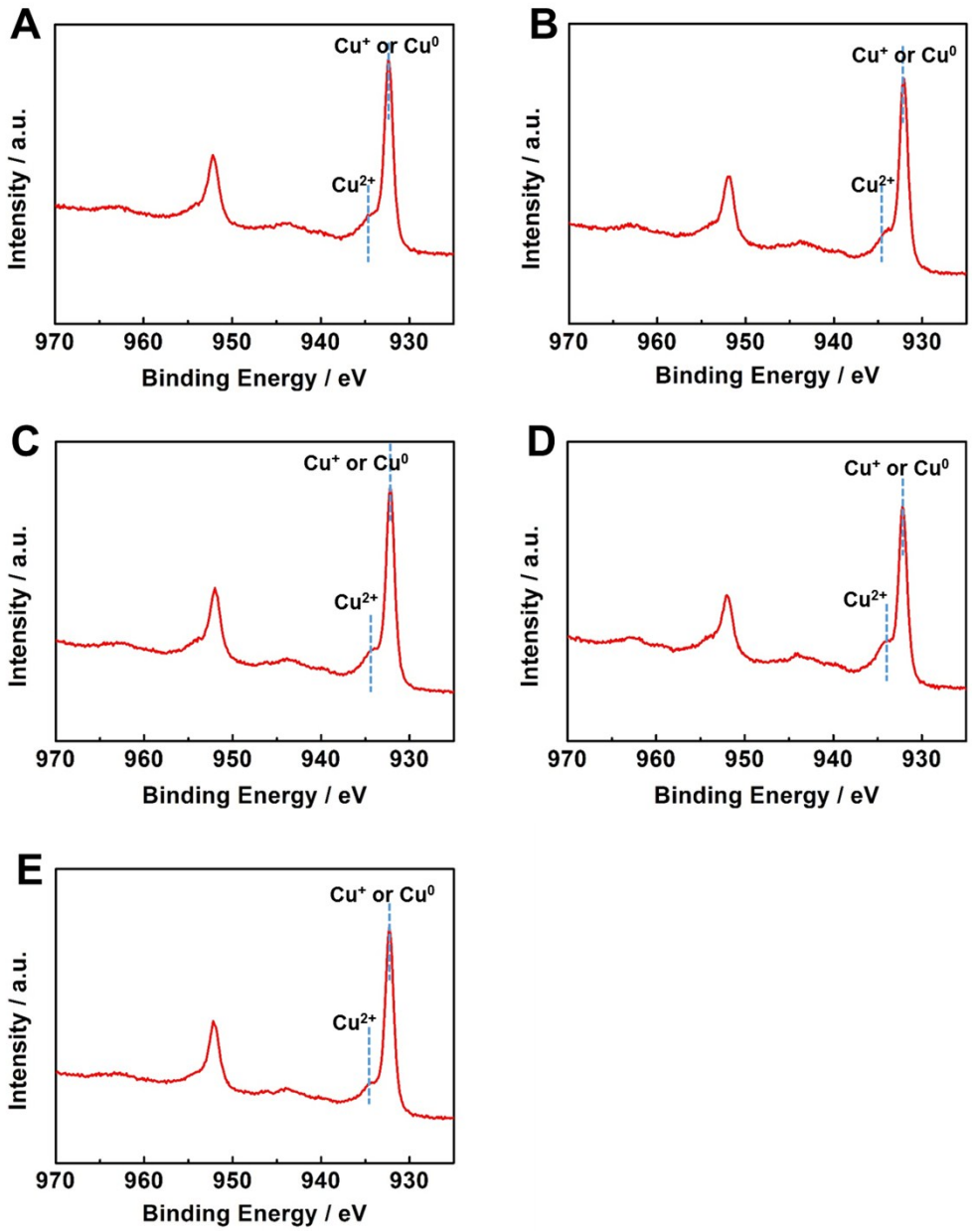

Figure S12. XPS spectra of Cu 2p orbits: R-Cu$(OH)_2$ (A), R-Cu-2 (B), R-Cu-5 (C), R-Cu-10 (D) and R-Cu-20 (E).

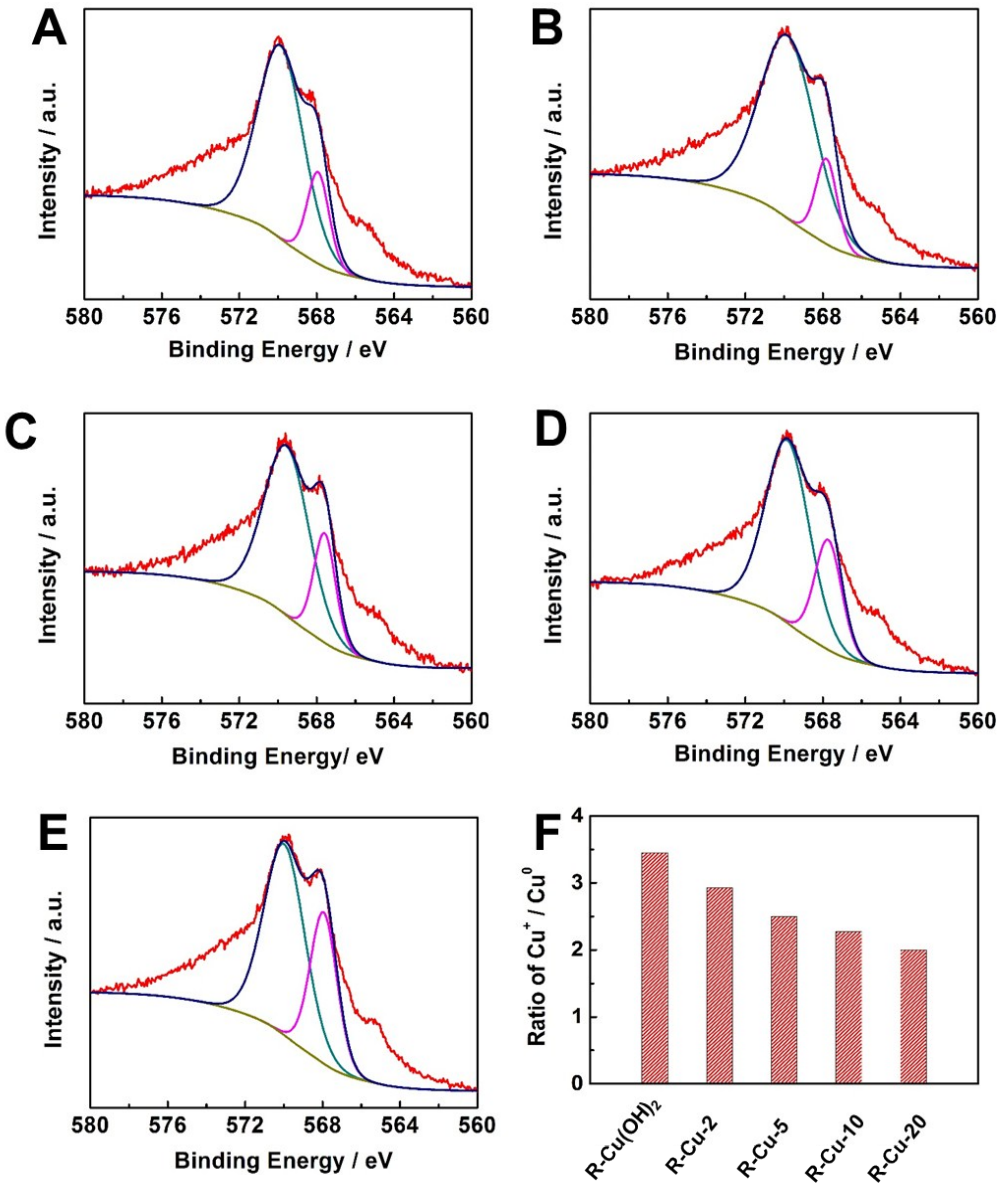

Figure S13. The fitting Auger Cu LMM line spectra: R-Cu$(OH)_2$ (A), R-Cu-2 (B), R-Cu-5 (C), R-Cu-10 (D), R-Cu-20 (E) and the ratios of Cu^+/Cu^0 over different R-Cu-x (F).

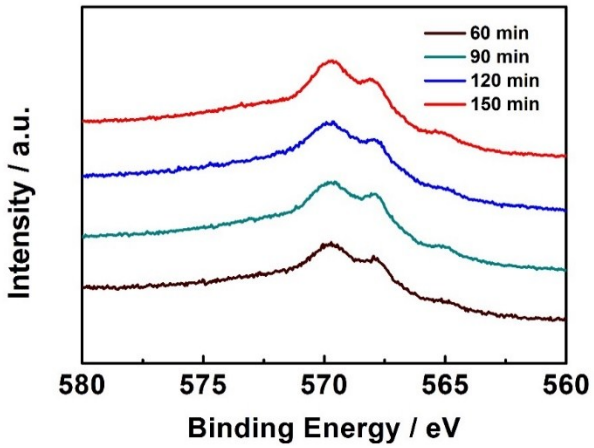

Figure S14. LMM Auger spectra of Cu for R-Cu-5 with different electrolysis time.

Supplementary Tables

Table S1. The onset potential of C2 products over R-Cu-x catalysts.

Catalysts	Ethane(V vs. RHE)	ethanol(V vs. RHE)	ethylene(V vs. RHE)
R-Cu$(OH)_2$	-0.79	-0.78	-0.82
R-Cu-2	-0.73	-0.74	-0.76
R-Cu-5	-0.45	-0.50	-0.51
R-Cu-10	-0.45	-0.51	-0.53
R-Cu-20	-0.72	-0.73	-0.74

Table S2. Comparision of Optimized C2+ products on various Cu-based catalysts.

Samples	Substrate	electrolyte	E vs. RHE	FEC2+ (%)	references
R-Cu-5	Cu plate	0.1M $KHCO_3$	-0.9	64.5	This work
Cu_2O NP/C	Glassy carbon	0.1M $KHCO_3$	-1.1	74.0	S4
copper from a sol-gel	Carbon paper	0.1M $KHCO_3$	-1.2	52.9	S5
Cu_2O-derived Cu NPs	Cu plate	0.1M $KHCO_3$	-1.1	33.5	S6
Cu_2O-derived Cu NPs	Cu disc	0.1M $KHCO_3$	-1.0	48.1	S7
Cu_2O (Cl induced)	Cu disc	0.1M KCl	-1.8	55.1	S8
Cu_2O film (1.7μm)	Cu disc	0.1M $KHCO_3$	-0.99	47.9	S9
Mesoporous Cu_2O	Cu foam on Cu wafer	0.5M $NaHCO_3$	-0.8	55.0	S10
Mesocrystal Cu from CuCl film	Cu disc	0.1M $KHCO_3$	-0.99	27.2	S11
Agglomerated Cu nanocrystal	Cu disc	0.1M $KHCO_3$	-0.95	60.3	S12
Transformed Cu NP ensemble	Carbon paper	0.1M $KHCO_3$	-0.85	55.2	S13
Cu nanocube (44nm)	Glassy carbon	0.1M $KHCO_3$	-1.1	50.1	S14
Cu NPs (7nm)	Glassy carbon	0.1M $NaHCO_3$	-1.15	5	S15
Plasma-Copper Nanocube	Cu film	0.1M $KHCO_3$	-0.9	60	S16

Table S3. Comparision of C2+ products on various Cu-based catalysts at low potentials.

catalysts	Electrolyte	j（C2）/ mA cm^{-2}	FE（C2）/ %	Potential (V vs. RHE)	Reference
R-Cu-5	0.1M $KHCO_3$	2.3	22.5	-0.6	This work
R-Cu-5	0.1M $KHCO_3$	4.5	32.1	-0.7	This work
B-Oxide-derived copper	0.1M $KHCO_3$	2.2	27	-0.7	S1
Nanopores-Copper	0.1M $KHCO_3$	0	0	-0.7	S17
Oxide-Derived CuxZn	0.1M $KHCO_3$	0	0	-0.7	S18
Plasma-Copper Nanocube	0.1M $KHCO_3$	0.39	13	-0.7	S11
Amino acid modified copper	0.1M $KHCO_3$	0.1	3	-0.7	S19
Metal ion cycling of Cu foil	0.25M $KHCO_3$	1	8	-0.7	S20
copper from a sol-gel	0.1M $KHCO_3$	0.3	3	-0.7	S5
Bi-Phasic Cu_2O-Cu	0.1M $KHCO_3$	0.1	5	-0.7	S21
Highly Dense Cu Nanowires	0.1M $KHCO_3$	3	25	-0.7	S22
Mixed Copper States in Anodized Cu	0.1M $KHCO_3$	-	3	-0.7	S23

Table S4. The results of C_{dl} and roughness factor for different samples.

Catalysts	The slope (mF cm^{-2})	C_{dl} (mF cm^{-2})	roughness factor
R-$Cu(OH)_2$	34.4	17.2	1
R-Cu-2	36.8	18.4	1.07
R-Cu-5	47.0	23.5	1.37
R-Cu-10	41.7	20.9	1.21
R-Cu-20	37.5	18.8	1.09

Table S5. The Grain boundaries surface density for differnet samples.

catalysts	Grain boundaries surface density (μm^{-1})
R-$Cu(OH)_2$	12.7
R-Cu-2	36.9
R-Cu-5	64.8
R-Cu-10	86.4
R-Cu-20	57.2

References

S1 C. Chen, X. Sun, L. Lu, D. Yang, J. Ma, Q. Zhu, Q. Qian, B. Han, *Green Chem.* **2018**, *20*, 4579.

S2 X. Kang, Q. Zhu, X. Sun, J. Hu, J. Zhang, Z. Liu, B. Han, *Chem. Sci.* **2016**, *7*, 266.

S3 X. Feng, K. Jiang, S. Fan, M. W. Kanan, *J. Am. Chem. Soc.* **2015**, *137*, 4606.

S4 H. Jung, S. Y. Lee, C. W. Lee, M. K. Cho, D. H. Won, C. Kim, H. S. Oh, B. K. Min, Y. J. Hwang, *J. Am. Chem. Soc.* **2019**, *141*, 4624.

S5 P. De Luna, R. Quintero-Bermudez, C.-T. Dinh, M. B. Ross, O. S. Bushuyev, P. Todorović, T. Regier, S. O. Kelley, P. Yang, E. H. Sargent, *Nat. Catal.* **2018**, *1*, 103.

S6 R. Kas, R. Kortlever, A. Milbrat, M. T. M. Koper, G. Mul, J. Baltrusaitis, *Phys. Chem. Chem. Phys.* **2014**, *16*, 12194.

S7 C. S. Chen, J. H. Wan, B. S. Yeo, *J. Phys. Chem. C* **2015**, *119*, 26875.

S8 D. Kim, S. Lee, J. D. Ocon, B. Jeong, J. K. Lee, J. Lee, *Phys. Chem. Chem. Phys.* **2015**, *17*, 824.

S9 D. Ren, Y. L. Deng, A. D. Handoko, C. S. Chen, S. Malkhandi, B. S. Yeo, *ACS Catal.* **2015**, *5*, 2814.

S10 A. Dutta, M. Rahaman, N. C. Luedi, P. Broekmann, M. Mohos, *ACS Catal.* **2016**, *6*, 3804.

S11 D. F. Gao, I. Zegkinoglou, N. J. Divins, F. Scholten, I. Sinev, P. Grosse, B. R. Cuenya, *ACS Nano* **2017**, *11*, 4825.

S12 C. S. Chen, A. D. Handoko, J. H. Wan, L. Ma, D. Ren, B. S. Yeo, *Catal. Sci. Technol.* **2015**, *5*, 161.

S13 D. Kim, C. S. Kley, Y. F. Li, P. D. Yang, *Proc. Natl. Acad. Sci. U. S. A.* **2017**, *114*, 10560.

S14 A. Loiudice, P. Lobaccaro, E. A. Kamali, T. Thao, B. H. Huang, J. W. Ager, R. Buonsanti, *Angew. Chem., Int. Ed.* **2016**, *55*, 5789.

S15 D. Ren, N. T. Wong, A. D. Handoko, Y. Huang, B. S. Yeo, *J. Phys. Chem. Lett.* **2016**, *7*, 20.

S16 H. Mistry, A. S. Varela, C. S. Bonifacio, I. Zegkinoglou, I. Sinev, Y. W. Choi, K. Kisslinger, E. A. Stach, J. C. Yang, P. Strasser, B. R. Cuenya, *Nat. Commun.* **2016**, *7*, 12123.

S17 T. T. H. Hoang, S. Ma, J. I. Gold, P. J. A. Kenis, A. A. Gewirth, *ACS Catal.* **2017**, *7* , 3313.

S18 D. Ren, B. S.-H. Ang, B. S. Yeo, *ACS Catal.* **2016**, *6*, 8239.

S19 F. Li, S.-F. Zhao, L. Chen, A. Khan, D. R. MacFarlane, J. Zhang, *Energy Environ. Sci* **2016**, *9*, 216.

S20 K. Jiang, R. B. Sandberg, A. J. Akey, X. Liu, D. C. Bell, J. K. Nørskov, K. Chan, H. Wang, *Nat. Catal.* **2018**, *1*, 111.

S21 S. Lee, D. Kim, J. Lee, *Angew. Chem., Int. Ed.* **2015**, *54*, 14701.

S22 D. Raciti, K. J. Livi, C. Wang, *Nano Lett.* **2015**, *15*, 6829.

S23 S. Y. Lee, H. Jung, N. K. Kim, H. S. Oh, B. K. Min, Y. J. Hwang, *J. Am. Chem. Soc.* **2018**, *140*, 8681.